Phase transitions associated with competing order parameters in compressively strained $SrTiO_3$ thin films

Tomoaki Yamada,[1,2,3,*] Benjamin Wylie-van Eerd,[4] Osami Sakata,[3,5] Alexander K. Tagantsev,[6,7] Hitoshi Morioka,[3,8] Yoshitaka Ehara,[3] Shintaro Yasui,[3] Hiroshi Funakubo,[3] Takanori Nagasaki,[1] and H. J. Trodahl[4]

[1]*Department of Materials, Physics and Energy Engineering, Nagoya University, Furo-cho, Chikusa-ku, Nagoya 464-8603, Japan*

[2]*PRESTO, Japan Science and Technology Agency, 4-1-8 Honcho, Kawaguchi, Saitama 332-0012, Japan*

[3]*Department of Innovative and Engineered Materials, Tokyo Institute of Technology, Yokohama 226-8502, Japan*

[4]*MacDiarmid Institute for Advanced Materials and Nanotechnology, Victoria University of Wellington, New Zealand*

[5]*Synchrotron X-ray Station at SPring-8 and Synchrotron X-ray Group, National Institute for Materials Science, Sayo, Hyogo, 679-5148, Japan*

[6]*Ceramics Laboratory, EPFL-Swiss Federal Institute of Technology, CH-1015 Lausanne, Switzerland*

[7]*Ferroics laboratory, Ioffe Physical Technical Institute, 194021 St. Petersburg, Russia*

[8]*Application Laboratory, Bruker AXS, Yokohama 221-0022, Japan*

(Received 18 February 2014; revised manuscript received 6 May 2015; published 3 June 2015)

(100)-epitaxial $SrTiO_3$ thin films having biaxial compressive strains up to −1.60% were grown on lattice mismatched substrates. Two phase transitions induced by the coupled instabilities (antiferrodistortive and ferroelectric) in $SrTiO_3$ were revealed in a common set of samples investigated at temperatures from 8 to 600 K by CuKα and synchrotron x-ray diffractions and by UV-Raman spectroscopy. It is shown that the in-plane compressive strain in $SrTiO_3$ significantly increases the transition temperature between cubic and tetragonal-antiferrodistortive phases and furthermore precipitates a ferroelectric polar phase at lower temperatures. The strain-temperature phase diagram based on the measurements shows a cubic-to-antiferrodistortive transition temperature that is substantially higher than predicted within a phenomenological Landau-Ginsburg-Devonshire treatment. In contrast the transition to the ferroelectric polar phase is found to be close to the temperature predicted, with the consequence that there is no crossing of the two phase transitions for temperatures up to 600 K.

DOI: 10.1103/PhysRevB.91.214101 PACS number(s): 77.55.−g, 77.80.−e

I. INTRODUCTION

Ferroelectrics are ubiquitous in technology, based on their strong piezoelectric and pyroelectric responses, their nonlinear dielectric response, and their multistable polarization states. The vast majority of applications are based on polycrystalline $PbZr_xTi_{1-x}O_3$ (PZT) ceramics, but there is an ongoing interest in a search for alternatives, both for avoiding Pb in their manufacture and to find stronger responses [1,2]. One avenue available for exploration is by control of strain using high pressure. However, of equal fundamental interest and considerably more technological accessibility is the investigation of biaxial strain developed during the growth of crystals as thin films [3]. Here we focus on exactly such a system, investigating the existence of a ferroelectric polar phase in $SrTiO_3$ (STO) within a strain-temperature space.

STO adopts a conventional cubic perovskite phase at ambient temperature. Unlike many perovskites having an order parameter of ferroelectric polarization it does not pass through the various polar structures under reducing temperature, although it has been recognized for decades to be an incipient ferroelectric, showing many signs of an approaching ferroelectric state as the temperature is lowered toward 0 K [4,5]. High pressure has been shown to stabilize a ferroelectric phase in STO above 0 K, as have chemical and even isotopic substitutions [6–11]. The most spectacular example is the room temperature ferroelectricity in STO films strained by a large biaxial tension [3]. In these films, the ferroelectric transition with the in-plane polarization is expected and indeed has been experimentally identified from the soft mode behavior [12]. On the other hand, the ferroelectric transition with the out-of-plane polarization is expected in the compressively strained STO films, although the clear ferroelectric transition has been rarely reported [13,14].

In addition to the ferroelectric instability in STO, there is competing structural transition at 105 K, into a nonpolar tetragonal structure with alternately right-and left-rotated oxygen octahedra, an antiferrodistortive (AFD) phase. For some years there have been predictions relating to the phase stabilization by these two order parameters (instabilities) in STO under biaxial strain [15–17]. The competition between the two order parameters, polarization and rotation of oxygen octahedra, then lends special interest to this system; the potential to stabilize the ferroelectric phase at finite temperature raises the possibility that the two phase transition lines may in fact cross. One can expect an appreciable impact of the rotation of oxygen octahedra on the dielectric response in the vicinity of such a crossing point, which may result in useful properties for applications such as an improved temperature stability of relatively large dielectric constant. Even more generally such competing order parameters are of considerable current interest relating to a wide range of physical phenomena in condensed matter science.

A phenomenological thermodynamic treatment based on Landau-Ginsburg-Devonshire (LGD)-type theory suggests that the ferroelectric polar phase is expected for biaxial compressive strains of greater magnitude than −0.2% [15], with a transition temperature rising to almost 200 K for −1.1% strain, almost twice the AFD transition temperature in unstrained

*t-yamada@nucl.nagoya-u.ac.jp

STO (105 K). It also suggests that the AFD transition rises with compressive strain at a lower rate than the ferroelectric transition temperature, so that the two would be expected to cross at a temperature near 200 K at a biaxial strain of −1.1% [15].

There have been several experimental studies of the transition lines on the temperature-strain phase diagram of STO, although disagreement among them leaves a still confused situation. Direct structural observations, following the intensity of superlattice spots under unit cell doubling in the AFD phase, show the cubic-to-tetragonal AFD phase transition much higher in temperature than predicted for compressively strained STO films [18–20]. Independently, dielectric measurements on a compressed film supported the predicted phase line for the ferroelectric polar phase transition temperature, which then implies that there will be no crossing point [13]. There is even a report of the relaxor behavior without any clear ferroelectric transition in a similarly strained film, nowhere close to the crossing point [14]. In contrast there exists a report of a crossing point, based on an indirect investigation of the structural transitions as signaled by second harmonic generation under optical excitation [21]. However, one must also note the impact of the slight off-stoichiometry in STO films as it is known to sensitively affect the unit cell size and ferroelectricity [22,23], which complicates the matter and impacts on the reliable comparison among different films. To date there appear to be no systematic experiments that follow both transitions on a common set of strained films, which would then directly establish whether the phase lines do, in fact, cross.

In the present work we report a study of the phase transitions in STO films grown with in-plane compressive strains up to −1.6%. The films were investigated by a combination of temperature-dependent x-ray diffraction (XRD) and Raman spectroscopy techniques that will be seen to complement each other in revealing the transitions into the AFD and ferroelectric polar phases. It will be seen that we find no evidence of crossing transition lines, indeed the two remain separated by more than 100 K over the entire strain range investigated.

II. EXPERIMENTAL DETAILS

A. Film growth

STO thin films were deposited on $LaAlO_3$ (LAO) (100), (La,Sr)(Al,Ta) O_3 (LSAT) (100), $NdGaO_3$ (NGO) (110), and STO (100) substrates by pulsed laser deposition (PLD) with KrF excimer laser ($\lambda = 248$ nm). Stoichiometric STO single crystals were used as the targets. The deposition temperature and oxygen pressure during the deposition were in the range of $700 - 720\,^{\circ}$C and 1×10^{-4}–5×10^{-4} Torr.

Special care has been exercised to ensure that the films are well formed and stoichiometric with an equilibrium lattice constant that is the same as bulk STO, a_0; a lattice constant that differs from STO affects in turn the strain imposed by epitaxial growth on lattice mismatched substrates [24–27]. There are several possible sources for a deviation in unit cell size, but a slight off-stoichiometry is most likely [22,27,28]. Although it has been generally recognized that PLD can achieve a good stoichiometry of the films, dedicated optimizations are required to realize this. We have ensured stoichiometry by growing homo-epitaxial films on substrates of STO, and ensuring that the diffraction peaks from the film and the substrate overlap. To achieve the match we changed the laser energy density, following the optimization procedure as has been reported by Ohnishi *et al.* [22] This optimized condition for homo-epitaxial films, which yielded a difference in unit cell size of less than 0.02%, was then used in the growth of all the strained films in the study. Here, the unit cell size of the films is defined by taking into account the elastic deformation, as

$$a_0 = ((s_{11} + s_{12})a_{\perp} - 2s_{12}a_{||})/(s_{11} - s_{12}), \qquad (1)$$

where $a_{||}$ and $a_{\perp}$ are the in-plane and out-of-plane lattice constants of the films, and s_{ij} are the elastic compliance of STO.

The magnitude of the strain was controlled by selecting several mismatched substrates. The lattice mismatch increases in the order of 0, −0.95, −1.22 (average), and −2.97% for STO, LSAT, NGO, LAO substrates. In addition, in order to achieve more variations of strain, the films were grown with the different thicknesses, which results in the different strain relaxation states from the lattice mismatch.

B. XRD investigations

The lattice constant and symmetry, and their temperature dependence were investigated by XRD measurements performed using diffractometers with CuKα x rays (Philips X'Pert MRD, Bruker D8 DISCOVER, and D8 ADVANCE) and synchrotron radiation x rays (SPring-8, BL13XU beamline, Japan).

The in-plane and out-of-plane lattice constants at room temperature were precisely measured by reciprocal space mapping around STO 103 using CuKα1 x rays monochromated by Ge(220) 2-bounce crystal. The temperature dependence of the lattice constant was measured by θ-2θ scans of STO 002 peak in the range of 80–600 K using CuKα x rays.

A transition from the high temperature cubic phase to the tetragonal AFD phase was directly detected by additional superlattice peaks at half-integer index positions in XRD profiles. These arise from the symmetry change from space group $Pm\bar{3}m$ to $I4/mcm$, which involves the rotation of TiO_6 octahedra. The possible AFD transition within the tetragonal ferroelectric phase involving the rotation of TiO_6 octahedra can be also detected by the same measurement. Since the structural factors for those superlattice peaks are small, we used synchrotron radiation x rays with 12.4-keV photon energy (a wavelength of 0.1 nm). The temperature was controlled in the range of 90–530 K using the heater built into a Joule-Thomson refrigerator set in the chamber especially designed for the BL13XU beamline.

C. Raman spectroscopy

Raman spectra were collected with a Jobin-Yvon T64000 Raman spectrometer in triple-subtractive mode for maximum Rayleigh line rejection; 2400 line/mm diffraction gratings blazed for the near UV were used in all three of the dispersion stages of the spectrometer. The detection element was a liquid-nitrogen-cooled charge coupled device. The excitation, a

TABLE I. Labels for the observed Raman peaks in tetragonal polar phase of STO films on mismatched substrates: LAO, LSAT, and NGO.

Label	TO_2	TO_3	TO_4	LO_4
Frequency (cm^{-1})	175	265	550	800
Reference	[30]	[30]	[30]	[13]
LAO	○		○	○
LSAT	○		○	
NGO		○		○

325-nm line of a He-Cd gas laser, is above the interband absorption edge of STO, thus enhancing the film signal while suppressing scattering from substrates [29]. As a result, we are able to identify the films' vibrational modes in the UV Raman spectra, whereas the modes could not be seen at all in preliminary Raman spectra collected with visible-light excitation.

Spectra were collected from 8 K to ambient temperature. A Linkam THMS600 cryostat was situated on a microscope stage for temperatures above 80 K, and a UV microscope objective with numerical aperture 0.32 was used to collect the light in the back-scattering geometry. To access temperatures below 80 K we used a Janis CCS 450 helium cryostat. Due to the incompatibility of this cryostat with the microscope stage, these lower-temperature spectra were obtained in the pseudobackscattering geometry. The laser was focused onto the sample by a 150-mm focal-length lens and the scattered light was imaged at the spectrometer's entrance slit with a UV lens of numerical aperture 0.34 matched to the spectrometer focal ratio. We collected overlapping spectra from the two cryostats in the intermediate temperature range between 80 and 200 K.

Spectral signatures of the tetragonal polar phase of STO are conventionally labeled as TO_1 to TO_4 and their LO counterparts [9,13], and appear at the frequencies given in Table I. We have managed to access a subset of these in every one of the strained films, but masking by substrate spectra has prevented measurements based on a common line across all films. Figure 1 shows typical low-temperature spectra in which the most useful features are identified for films on each of the four substrate crystals. Below we use the temperature-dependent amplitudes of the polar-phase vibrational lines to assign transition temperatures [13,29,30]. Extracting the amplitudes is aided by fitting the lines to Lorentzian functions, and a Fano line to account for interference with a broad background signal in the case of TO_2. Corrections were made for the Bose factor.

It has been reported that very weak peaks of the polar-structure modes were observed in Raman spectra of unstrained polycrystalline STO ceramics, and were interpreted in terms of small polar-phase regions induced by grain boundaries and other structural defects [30–32]. We have investigated such a possibility in our films by seeking the polar-phase Raman signatures in an unstrained homoepitaxial 40-nm-thick film (STO/40). It is clear in Fig. 1 that there is no sign at all of the polar Raman lines at any temperature down to 9 K in the unstrained film, eliminating structural defects as the major cause for the polar STO modes in our spectra.

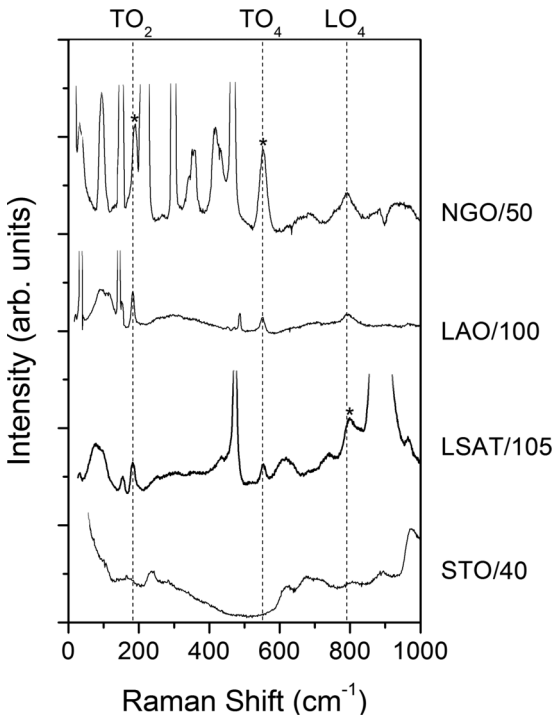

FIG. 1. Raman spectra of a range of samples showing each substrate used in the experiments. The spectra were all recorded at 9 K. The polar STO modes used to signal the polar phase are marked with dashed lines, and significant substrate lines that mask these modes are marked by *. The number in sample name represents the thickness of STO films in nm. The sample naming scheme and details are described in the Table II caption.

III. RESULTS AND DISCUSSION

A. Strain measurement

Table II shows the room temperature lattice constants and strain of STO films employed in this study. The in-plane strain $u_{||}$, and out-of-plane strain $u_{\perp}$, were defined as

$$u_{||} = (a_{||} - a_0)/a_0 \quad \text{and} \quad u_{\perp} = (a_{\perp} - a_0)/a_0, \qquad (2)$$

where $a_{||}$ and $a_{\perp}$ are the in-plane and out-of-plane lattice constants and $a_0 = 3.905$ Å at room temperature. The in-plane and out-of-plane lattice constants of the film homo-epitaxially grown on STO substrate (STO/40) are the same within the uncertainty as a_0, confirming excellent stoichiometry in the films deposited under the conditions in this study. Otherwise the films are all in-plane compressed due to the negative lattice mismatch between film and substrate. As shown in the table, the in-plane compressive strain was larger for larger lattice mismatch and thinner films, so that the largest strain of -1.60% and the smallest strain of -0.24% were achieved for the 30-nm-thick film on LAO (LAO/30) and the 140-nm-thick film on LSAT (LSAT/140), respectively. The observed strains were larger than the previously reported values by He *et al.* [20] for the similar film thicknesses and the same substrates. We believe this is a result of the lower oxygen pressure during PLD slowing the strain relaxation process during the hetero-epitaxial growth. It should be noted that the film on

TABLE II. Room temperature lattice constants and strains of the STO films used in this study. The sample names identify the substrate and the film thicknesses in nm. The error of the estimated in-plane and out-of-plane strain is ±0.08% and ±0.03%, respectively.

			Lattice constant (Å)		Strain (%)	
Sample	Film thickness (nm)	Substrate	$a_{\|\|}$	$a_{\perp}$	$u_{\|\|}$	$u_{\perp}$
LAO/30	30	LAO	3.842	3.953	−1.60	1.24
LAO/100	100	LAO	3.878	3.928	−0.69	0.59
LSAT/60	60	LSAT	3.869	3.933	−0.92	0.71
LSAT/105	105	LSAT	3.871	3.929	−0.87	0.62
LSAT/140	140	LSAT	3.896	3.911	−0.24	0.16
NGO/50	50	NGO	3.863/3.854	3.948	−1.08/−1.31	1.10
STO/40	40	STO	3.905	3.906	0.00	0.03

NGO is strained anisotropically in-plane due to the rectangular net presented by the NGO (110) surface.

In addition to the difference in the strain between different films, it should be noticed that the strain of thicker films is inhomogeneous because of the partial relaxation state from the lattice mismatch caused by several factors that prevent formation of misfit dislocations [33–35]. Figure 2 shows XRD reciprocal space maps for the films on LSAT with different film thicknesses as typical results showing the partial strain relaxation. Qx and Qz are the inverse of lattice spacing in the in-plane and out-of-plane directions, respectively. As can be clearly seen, the in-plane lattice spacing of the thinnest film (LSAT/60) matches that of the LSAT substrate; therefore, the film is fully constrained and the strain is uniform throughout the film. On the other hand, the thicker films (LSAT/105, LSAT/140) are partially relaxed; therefore, there are wide variations of the strain. Figure 3 shows the STO 103 peak profiles with respect to Qx, for which the intensity is integrated along the Qz direction. As drawn in the figures, the strain variation of thicker films would be decomposed into two parts for simplicity. Since the strain relaxation most likely starts at the growing surface for the examined heterostructures [33], the residual strain remains large near the film/substrate interfaces and becomes small in the upper part of the films.

Figure 4 shows the in-plane and out-of-plane strains for the films used in this study. As discussed above, the strain of the partially relaxed films has variation for constrained and relaxed regions. The strain of LAO/100 is, however, plotted without variation, as the constrained region is almost undetectable due to the considerable relaxation from the large mismatch between STO and LAO (−2.97%). As for NGO/50, two kinds of in-plane strain are plotted due to the rectangular net of the NGO (110) surface although the film is almost fully constrained. Except for the homo-epitaxial film (STO/40), the out-of-plane strains are basically always positive (tensile) due to the elastic deformation by the in-plane negative (compressive) strain. If the films are in the paraelectric cubic phase at room temperature as bulk STO, the in-plane strain $u_{||}$, and out-of-plane strain $u_{\perp}$, should obey the relationship,

$$u_{\perp} = u_{||}(2s_{12}/(s_{11} + s_{12})), \tag{3}$$

shown as the filled area in the figure. As can be seen, the in-plane strain and out-of-plane strain of the films have nearly

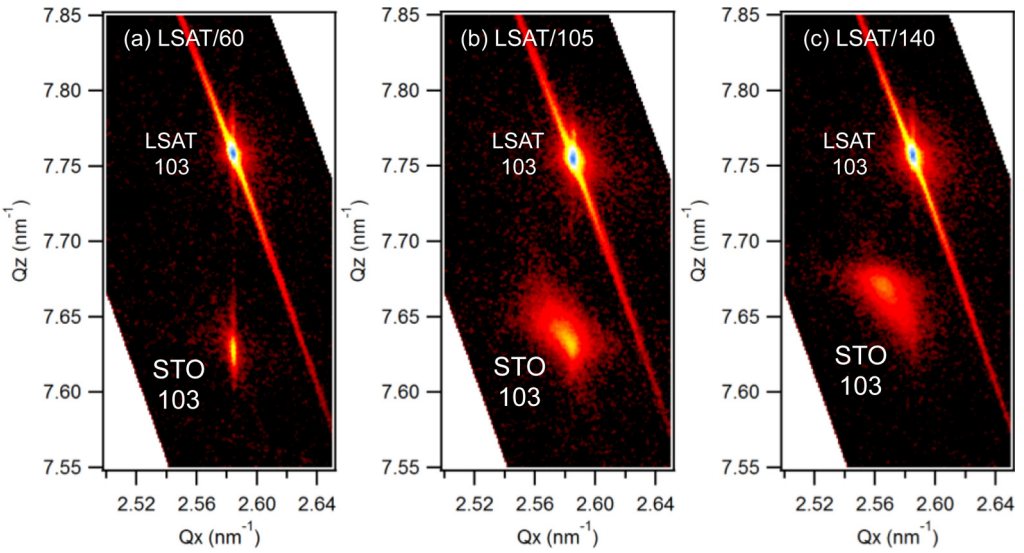

FIG. 2. (Color online) XRD reciprocal space maps around STO 103 reflections for the samples (a) LSAT/60, (b) LSAT/105, and (c) LSAT/140.

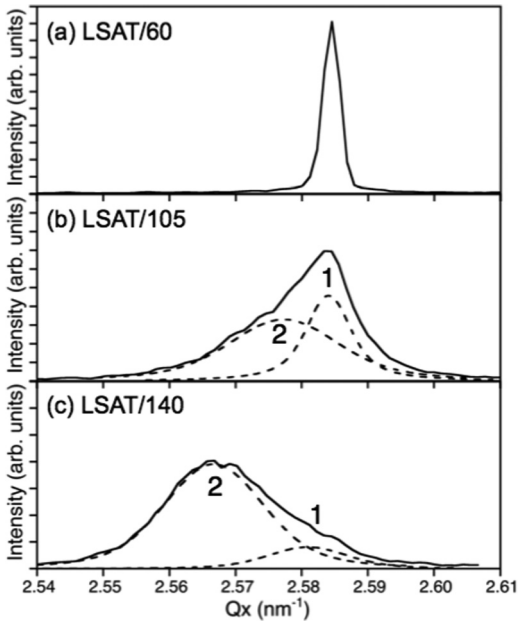

FIG. 3. STO 103 peak profiles with respect to Qx for the samples (a) LSAT/60, (b) LSAT/105, and (c) LSAT/140. The peak intensity is integrated along the Qz direction. Dashed lines show the decomposed profiles for the constrained (1) and relaxed (2) regions.

a proportional relationship, although their slope is somewhat larger than the theoretical slope for the paraelectric cubic phase taking into account the elastic deformation. Specifically, the deviation of the out-of-plane strain from the theoretical line becomes larger for the larger in-plane strain. This may be due to the elongation of the lattice by the rotation of the oxygen octahedra and/or the spontaneous polarization [36,37].

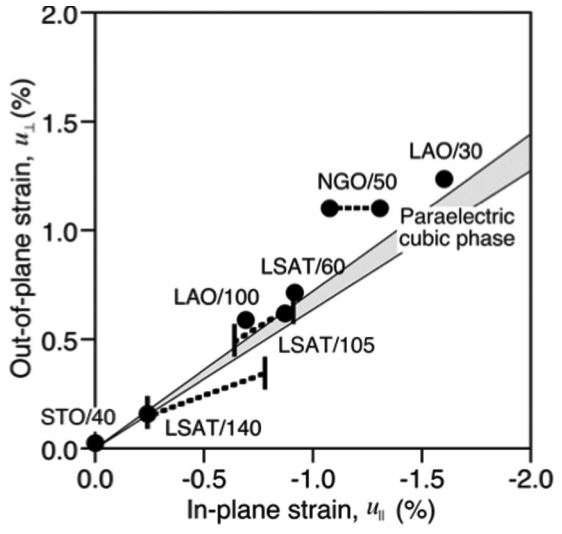

FIG. 4. Ambient-temperature in-plane strain and out-of-plane strain of the samples. The strains of partially relaxed LSAT/105 and LSAT/140 are plotted with dashed lines showing the variation of the strain. The two in-plane strains are plotted for NGO/50 due to the rectangular net of the NGO (110) surface. The filled area represents the out-of-plane strain that would follow from the Poisson ratio in the paraelectric cubic phase.

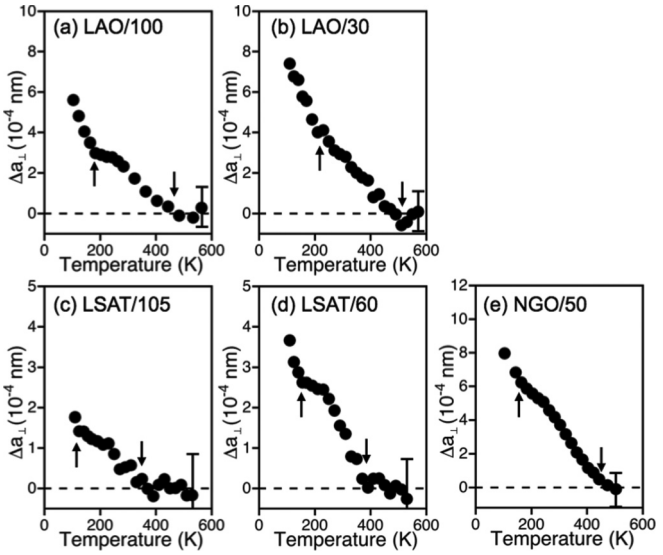

FIG. 5. Deviation of the out-of-plane lattice constant from that expected for the HT phase for the samples: (a) LAO/100, (b) LAO/30, (c) LSAT/105, (d) LSAT/60, and (e) NGO/50. The error bars represent a systematic uncertainty. The arrows indicate the temperatures at which there are sudden rises in the lattice constant, to be associated with the expected phase changes.

B. Temperature-dependent XRD, the structural phase transitions

The temperature dependence of the lattice constant gives a signature of phase transitions because both transitions involving the two order parameters in STO, the rotation of oxygen octahedra and the spontaneous polarization, result in the elongation of the lattice along these axes. As is well established, for the compressively strained STO (100) films, the elongated c axes in both phases lie perpendicular to the substrate surface [13,15,20]. Thus the phase transition temperatures are signaled by sudden elongation of the substrate-normal lattice constant when the temperature is lowered into the AFD and ferroelectric polar phases. Figure 5 shows the temperature dependence of the out-of-plane lattice constant for the films on LAO, LSAT, and NGO substrates as typical results, plotted as the deviation from the expected out-of-plane lattice constant of the high temperature paraelectric cubic phase (HT phase),

$$\Delta a_{\perp}(T) = a_{\perp}(T) - a_{\perp HT}(T). \quad (4)$$

Here, $a_{\perp HT}(T)$ is the expected out-of-plane lattice constant adjusted to account for the lattice distortion imposed by the in-plane biaxial strain $u_{||}(T)$; namely,

$$a_{\perp HT}(T) = a_{0HT}(T)(1 + u_{||}(T)(2s_{12}/(s_{11} + s_{12}))), \quad (5)$$

where $a_{0HT}(T)$ is the lattice constant of unstrained STO in cubic phase at the given temperature. $u_{||}(T)$ over the whole temperature range was estimated from the temperature dependence of lattice constant of the substrates and the precise lattice constant of the films at room temperature assuming that the in-plane lattice constant of the films is clamped by the substrate. In all the films the high-temperature data are clustered about zero within the $\sim 10^{-5}$ nm scatter, but they

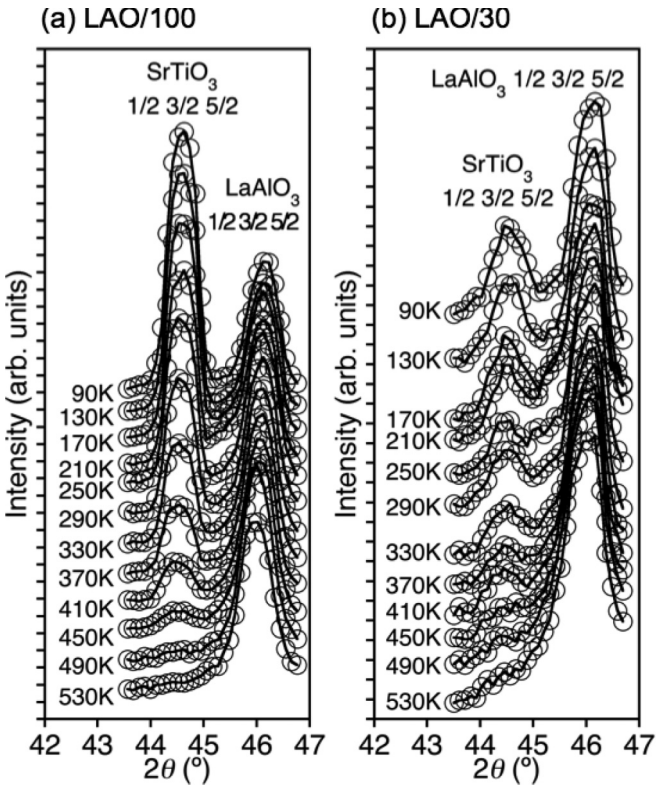

FIG. 6. Temperature dependence of XRD profiles at a half-integer index position of STO 135 reflections for the samples (a) LAO/100 and (b) LAO/30.

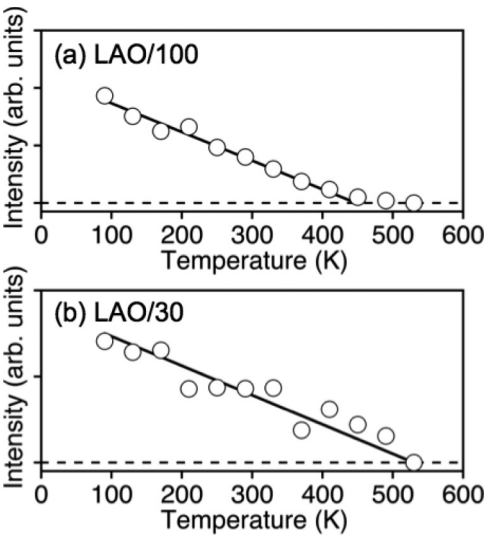

FIG. 7. Temperature dependence of the STO 1/2 3/2 5/2 peak intensity for the samples (a) LAO/100 and (b) LAO/30.

also all show a clear increasing lattice constant in the range of 300–500 K. In four of the films (LAO/100, LAO/30, LSAT/60, and NGO/50) there is another clear increase below 210 K, and in LSAT/105, the lowest-temperature point appears to be the start of an increasing lattice constant. Thus already this measurement signals two widely separated transition temperatures, as marked by the arrows in Fig. 5. However, these data alone do not identify which transition, into the AFD or ferroelectric polar phase, can be assigned to the two temperatures.

In order to determine the order parameter responsible for these transitions, the structural AFD transition owing to the rotation of TiO_6 octahedra was first investigated by observing the additional superlattice peaks at a half-integer index position in synchrotron XRD profiles. Figure 6 shows the temperature dependence of XRD profiles at a half-integer index position of LAO/100 and LAO/30 samples. In addition to the LAO 1/2 3/2 5/2 peak [38], a reflection corresponding to STO 1/2 3/2 5/2 was observed. As can be found in the figures, the intensity of STO 1/2 3/2 5/2 peak decreased with increasing temperature. Figure 7 shows the temperature dependence of the STO 1/2 3/2 5/2 peak intensity for those films. As shown in the figures, the peak intensity shows a monotonic decrease with rising temperature and meets zero at 450 K and 530 K for LAO/100 and LAO/30, respectively, indicating the un-rotated state of TiO_6 octahedra above these temperatures. As shown in Fig. 5, these films showed two transition temperatures in the temperature dependence of the lattice constant: 170 and 460 K for LAO/100, and 210 and 510 K for LAO/30. It is therefore clear that the appearance of the superlattice peak corresponds to the higher temperature transition.

In spite of the power of synchrotron XRD for exploring the cubic-to-tetragonal AFD structural phase transition, it is limited to substrates that display no interfering XRD peaks. For the films on LSAT and NGO, the peaks from the film and the substrate overlap, thus it is not able to decompose them. Nevertheless, we previously investigated the rotation of TiO_6 octahedra for the 35-nm-thick film on LSAT by the selected area electron diffraction using transmission electron microscopy in combination with the temperature dependence of the lattice constant [39], which supports that the rotation of TiO_6 octahedra is responsible for the higher temperature transition.

C. Raman spectroscopy, the ferroelectric polar phase transition

The assignment of the lower temperature feature in Fig. 5 to the transition to the ferroelectric polar phase, and a refined determination of the transition temperature, have been achieved with Raman spectroscopy. Figure 8 shows the temperature-dependent Raman spectra from sample LAO/100, in which the modes TO_2, TO_4, and LO_4 of the STO tetragonal polar phase all appear below about 200 K and strengthen as the temperature is lowered further. The amplitudes of the three strongest modes are plotted vs temperature in Fig. 9. It can be seen that all three modes show the same temperature dependence. We have used such plots to estimate the transition temperature below.

In Fig. 10, we show the peak intensities of the strongest polar-phase mode from three films: LAO/30, LAO/100, and LSAT/60. The peaks appear only below ambient temperature; they grow slowly upon lowering the temperature followed by a rapid increase and saturation as 0 K is approached. The rapid rise certainly signals an increase in the polar distortion, corresponding to an increasing order parameter. As expected the temperature where the maximum slope is achieved varies among the films. The very much weaker and relatively slowly varying signal that remains at higher temperature suggests

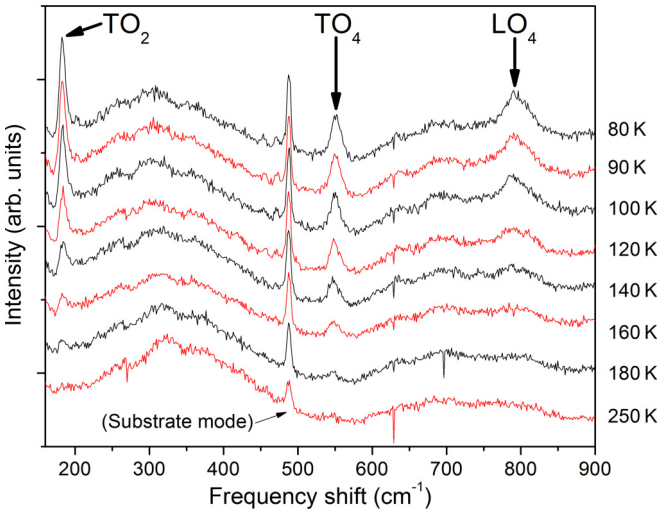

FIG. 8. (Color online) Raman spectra for sample LAO/100 from 80 to 250 K showing the appearance and strengthening of the polar STO modes, as marked.

a low density of polar regions that are retained above the transition, which we discuss below. In no case does the high-temperature tail exceed 10% of the 9-K amplitude. Thus to estimate a phase transition temperatures for the major fraction of the films we extrapolate a straight line, which is legitimate for the second-order phase transitions, drawn through the steepest slope to the intensity well above the transition.

The film on NGO presents special problems, since the TO_2 and TO_4 features are all but obscured by substrate lines. We thus have turned to LO_4 near 800 cm^{-1}. This line is clearly visible in all of the samples (Fig. 1) but it is broader

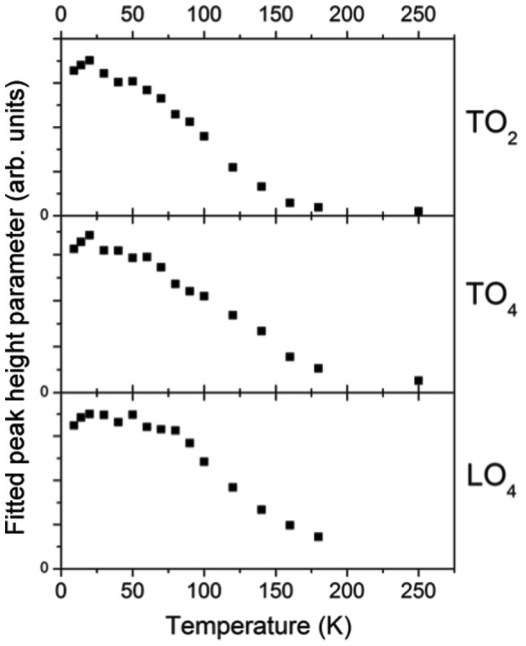

FIG. 9. Peak intensity vs temperature for three different polar modes in the same sample, LAO/100. It can be seen that the modes have almost identical temperature dependence.

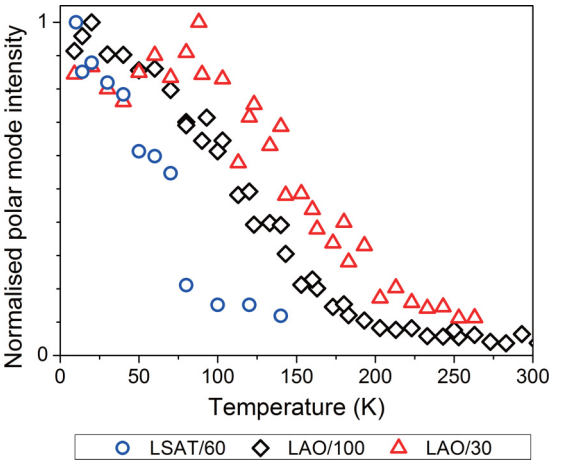

FIG. 10. (Color online) Polar mode intensity vs temperature in three different samples with different strain conditions, LAO/30, LAO/100, and LSAT/60 showing variation in phase transition temperature.

(50 cm^{-1}) and weaker than TO_2 and TO_4, and the intensity is not as clearly followed. It is further compromised by an even broader (150 cm^{-1}) STO second-order band lying directly under it. Nonetheless the data show a rapid reduction in the LO_4 line's intensity above 100 K, so that the composite LO_4 plus second-order feature loses amplitude and increases its apparent width. In order to characterize these changes and identify the temperature at which the LO_4 line weakens we fitted the composite line in NGO/50 with a single Lorentzian. The transition is then signaled by a rapid strength reduction concomitant with a width increase at 140–160 K, as seen in Fig. 11. The film clearly undergoes a transition to the FE polar phase in this temperature range.

This film shows an additional feature visible above the substrate at around 40 cm^{-1} (Fig. 12) that is masked by substrate features in the other substrates. This is a recognized mode in the AFD structure of STO, showing clear softening as the AFD-cubic phase transition is approached [9]. At temperatures above 160 K this is a single peak in our film NGO/50, immediately identifying the film as in the AFD phase above the 160-K transition. We have been unable to follow

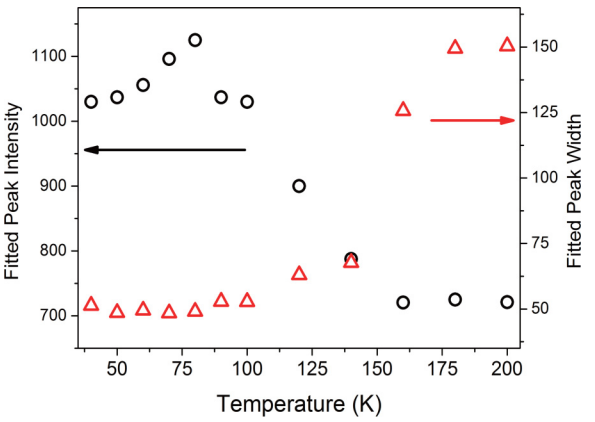

FIG. 11. (Color online) Fitting parameters for the NGO/50 LO_4 peak, showing a phase transition near 150 K by rapid change in both the intensity and the width of the peak.

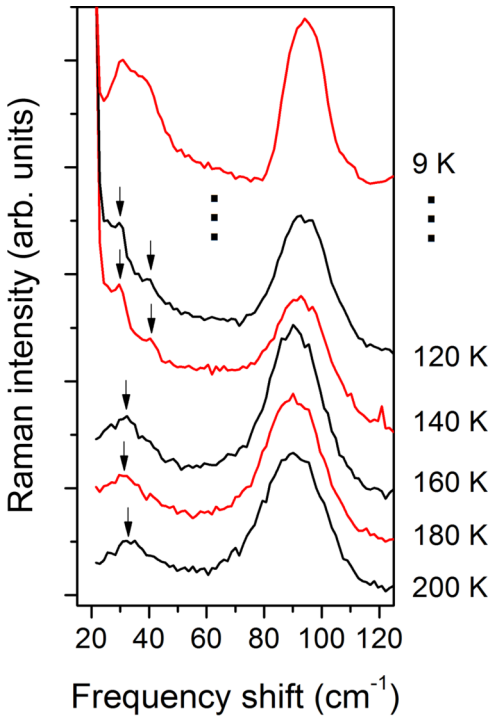

FIG. 12. (Color online) Raman spectra of NGO/50 showing the splitting of the AFD mode below 160 K. The mode discussed is marked by arrows.

lines at such low frequency to temperatures above 300 K in these thin films, which has prevented a Raman confirmation of the AFD-cubic transition seen in the XRD results. On the other hand, the line shows a clear signature of a structural phase transition at 160 K, where it splits discontinuously into two peaks. Such a splitting has also been reported across an AFD-to-ferroelectric polar transition in Ca-doped STO and $SrTi(^{18}O_x^{16}O_{1-x})_3$ [9,11]. Thus both the LO_4 line and the splitting of the 40 cm^{-1} line are in full agreement, giving a 160-K temperature for the AFD-to-ferroelectric polar transition in this film.

In none of the films do we find that the polar-phase lines vanish rigorously at a closely constrained transition temperature; as mentioned above there remains a weak and more slowly weakening remnant of their polar signal extending to temperatures well above the transition temperature. This includes a contribution from more strongly strained layers near the substrates; note that as is usual for strained films, most of the films show some degree of relaxation so that their typical lattice strain is somewhat less than the STO/substrate lattice mismatch. On the other hand, there is a literature reporting some of these Raman features being activated weakly by polar distortions centered on chemical defects, stacking faults and grain boundaries. Furthermore there is a prediction that polar structures may occur at antiphase boundaries in the AFD phase of STO [40]. These effects could also contribute to the weak remnant polar signal in our spectra.

D. The phase diagram

The full set of temperature-dependent XRD lattice-constant and superlattice measurements, combined with the signatures of a polar phase in Raman spectra, finally permits a construction of a phase diagram for STO under biaxial strain. The focus then is to investigate the transition temperatures into the AFD and ferroelectric polar phases to establish whether they are in agreement with predictions based on an LGD free-energy expansion, and in particular seek evidence of a crossing of the two transition lines near −1.1% biaxial strain.

Table III lists the transition temperatures for the films examined in this study. By comparing to the results of the Raman measurements, low temperature transitions observed in the temperature dependence of the lattice constant by XRD are corresponding to the ferroelectric transition. The high temperature transitions are thus assigned to be AFD transitions, as was also supported by the synchrotron superlattice measurement for some films. Figure 13 plots the strain-temperature phase diagram constructed from these data. The theoretical transition temperatures estimated by LGD-type theory are also drawn [15]. As can be seen, the observed AFD transition temperatures are substantially higher than the theoretical predictions and seem to be similar to the experimental results on STO films on LAO substrates reported by He *et al.* [20]. On the other hand, the ferroelectric transition temperatures follow more closely the theoretical predictions although some films showed appreciable deviations.

Our comprehensive measurements show quite conclusively that the compressively strained STO films, carefully grown under optimized conditions, do not show the crossing of the phase transition temperatures involving the rotation of the oxygen octahedra and the ferroelectric polarization. In addition, the observed tendency of the transition temperature vs strain suggests that no crossing point can be expected

TABLE III. Observed transition temperatures to the AFD and ferroelectric (FE) phases.

Sample	Film thickness (nm)	Substrate	$u_{\|\|}$ at RT (%)	AFD transition (K) XRD (lattice constant)	AFD transition (K) XRD (superlattice)	FE transition (K) XRD (lattice constant)	FE transition (K) UV-Raman
LAO/30	30	LAO	−1.60	510 ± 20	530 ± 40	210 ± 20	210 ± 15
LAO/100	100	LAO	−0.69	460 ± 40	450 ± 40	170 ± 20	170 ± 15
LSAT/60	60	LSAT	−0.92	370 ± 20	×	155 ± 20	130 ± 15
LSAT/105	105	LSAT	−0.87	270 ± 20	×	120 ± 20	90 ± 15
LSAT/140	140	LSAT	−0.24	270 ± 20	×	<80	90 ± 15
NGO/50	50	NGO	−1.08/−1.31	440 ± 40	×	160 ± 40	160 ± 10
STO/40	40	STO	0.00	105 ± 20	105 ± 5	–	–

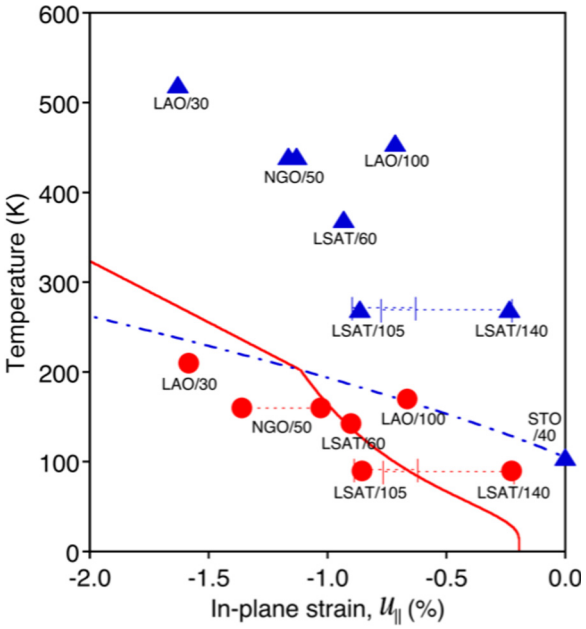

FIG. 13. (Color online) Strain-temperature phase diagram for compressively strained STO films. Blue triangles and red circles show the transition temperature to AFD phase and FE phase, respectively. The transition temperatures observed by multiple methods for the same samples are averaged. The strains of thicker films (LSAT/105 and LSAT/140) are shown with bars, reflecting the distribution of the strain. The theoretical lines for these transitions are also drawn as blue dot-dash and red solid lines, respectively.

even for stronger strains. The most likely explanation of the disagreement is that the LGD expansion coefficients are based on empirical data near ambient pressure, and represent here a possibly inaccurate extrapolation.

IV. CONCLUSIONS

We have grown (100)-epitaxial thin films of STO under a range of biaxial strain conditions by PLD, and have followed the cubic paraelectric-to-tetragonal antiferrodistortive-to-ferroelectric polar phase transitions in a common set of samples. A strain-free homoepitaxial film deposited in exactly the same way is shown to be substantially free of defects and to have excellent stoichiometry. XRD measurements of the temperature dependence of lattice constants implied the existence of two phase transitions in the biaxially compressed films. Synchrotron XRD confirmed the character of the higher temperature phase transition as cubic paraelectric-to-tetragonal AFD by detection of a superlattice peak in reciprocal space. Raman spectra further confirm the character of the lower temperature phase transition as AFD-to-ferroelectric by detection of polar STO vibrational modes and by splitting in the ferroelectric phase of a degenerate AFD mode. From the phase diagram thus deduced, it is clear that there is no crossing of the AFD and ferroelectric polar distortions in the measured range, in disagreement with the predicted behavior, and the gradient of the experimental lines suggest that such a crossing will not occur at any point in the phase diagram. The disagreement likely signals inaccurate LGD expansion coefficients. It is important that these widely used coefficients, evaluated 40 years ago, should be revisited.

ACKNOWLEDGMENTS

This work has been partially supported by MEXT/JSPS KAKENHI, Japan (Grants No. 18310085, No. 20510113, No. 20860036, No. 22015007, and No. 22760510). The research in the MacDiarmid Institute is supported by the New Zealand Centre of Research Excellence fund. The work of A.K.T. was supported by a grant from the government of Russian Federation 2012-220-03-434, Contract No. 14.B25.31.0025 and EU-FP7th IRSES project 'NANOCOM" (No. 269140). The synchrotron radiation experiments were performed at the BL13XU of SPring-8 with the approval of the Japan Synchrotron Radiation Research Institute (JASRI) (Proposals No. 2010A1522 and No. 2014A1499). T.Y. thanks Professor T. Kiguchi for discussion of the previous result of the film on LSAT.

[1] Y. Saito, H. Takao, T. Tani, T. Nonoyama, K. Takatori, T. Homma, T. Nagaya, and M. Nakamura, Nature (London) **432**, 84 (2004).
[2] M. D. Maeder, D. Damjanovic, and N. Setter, J. Electroceramics **13**, 385 (2004).
[3] J. H. Haeni, P. Irvin, W. Chang, R. Uecker, P. Reiche, Y. L. Li, S. Choudhury, W. Tian, M. E. Hawley, B. Craigo, A. K. Tagantsev, X. Q. Pan, S. K. Streiffer, L. Q. Chen, S. W. Kirchoefer, J. Levy, and D. G. Schlom, Nature (London) **430**, 758 (2004).
[4] T. Sakudo and H. Unoki, Phys. Rev. Lett. **26**, 851 (1971).
[5] K. A. Müller and H. Burkard, Phys. Rev. B **19**, 3593 (1979).
[6] W. J. Burke, R. J. Pressley, and J. C. Slonczewski, Solid State Commun. **9**, 121 (1971).
[7] W. J. Burke and R. J. Pressley, Solid State Commun. **9**, 191 (1971).
[8] H. Uwe and T. Sakudo, Phys. Rev. B **13**, 271 (1976).
[9] U. Bianchi, W. Kleemann, and J. G. Bednorz, J. Phys. Condens. Matter **6**, 1229 (1994).
[10] M. Itoh, R. Wang, Y. Inaguma, T. Yamaguchi, Y. J. Shan, and T. Nakamura, Phys. Rev. Lett. **82**, 3540 (1999).
[11] H. Taniguchi, T. Yagi, M. Takesada, and M. Itoh, Phys. Rev. B **72**, 064111 (2005).
[12] D. Nuzhnyy, J. Petzelt, S. Kamba, P. Kužel, C. Kadlec, V. Bovtun, M. Kempa, J. Schubert, C. M. Brooks, and D. G. Schlom, Appl. Phys. Lett. **95**, 232902 (2009).
[13] H. W. Jang, A. Kumar, S. Denev, M. D. Biegalski, P. Maksymovych, C. W. Bark, C. T. Nelson, C. M. Folkman, S. H. Baek, N. Balke, C. M. Brooks, D. A. Tenne, D. G. Schlom, L. Q. Chen, X. Q. Pan, S. V. Kalinin, V. Gopalan, and C. B. Eom, Phys. Rev. Lett. **104**, 197601 (2010).
[14] D. Nuzhnyy, J. Petzelt, S. Kamba, X. Martí, T. Čechal, C. M. Brooks, and D. G. Schlom, J. Phys. Condens. Matter **23**, 045901 (2011).

[15] N. A. Pertsev, A. K. Tagantsev, and N. Setter, Phys. Rev. B **61**, R825 (2000); **65**, 219901(E) (2002).
[16] Y. L. Li, S. Choudhury, J. H. Haeni, M. D. Biegalski, A. Vasudevarao, A. Sharan, H. Z. Ma, J. Levy, V. Gopalan, S. Trolier-McKinstry, D. G. Schlom, Q. X. Jia, and L. Q. Chen, Phys. Rev. B **73**, 184112 (2006).
[17] C. H. Lin, C. M. Huang, and G. Y. Guo, J. Appl. Phys. **100**, 084104 (2006).
[18] F. He, B. O. Wells, S. M. Shapiro, M. v. Zimmermann, A. Clark, and X. X. Xi, Appl. Phys. Lett. **83**, 123 (2003).
[19] F. He, B. O. Wells, Z. G. Ban, S. P. Alpay, S. Grenier, S. M. Shapiro, W. Si, A. Clark, and X. X. Xi, Phys. Rev. B **70**, 235405 (2004).
[20] F. He, B. O. Wells, and S. M. Shapiro, Phys. Rev. Lett. **94**, 176101 (2005).
[21] S. Denev, A. Kumar, M. D. Biegalski, H. W. Jang, C. M. Folkman, A. Vasudevarao, Y. Han, I. M. Reaney, S. Trolier-McKinstry, C. B. Eom, D. G. Schlom, and V. Gopalan, Phys. Rev. Lett. **100**, 257601 (2008).
[22] T. Ohnishi, K. Takahashi, M. Nakamura, M. Kawasaki, M. Yoshimoto, and H. Koinuma, Appl. Phys. Lett. **74**, 2531 (1999).
[23] D. A. Tenne, A. K. Farrar, C. M. Brooks, T. Heeg, J. Schubert, H. W. Jang, C. W. Bark, C. M. Folkman, C. B. Eom, and D. G. Schlom, Appl. Phys. Lett. **97**, 142901 (2010).
[24] E. J. Tarsa, E. A. Hachfeld, F. T. Quinlan, J. S. Speck, and M. Eddy, Appl. Phys. Lett. **68**, 490 (1996).
[25] C. M. Carlson, P. A. Parilla, T. V. Rivkin, J. D. Perkins, and D. S. Ginley, Appl. Phys. Lett. **77**, 3278 (2000).
[26] D. Fuchs, C. W. Schneider, R. Schneider, and H. Rietschel, J. Appl. Phys. **85**, 7362 (1999).
[27] T. Yamada, J. Petzelt, A. K. Tagantsev, S. Denisov, D. Noujni, P. K. Petrov, A. Mackova, K. Fujito, T. Kiguchi, K. Shinozaki, N. Mizutani, V. O. Sherman, P. Muralt, and N. Setter, Phys. Rev. Lett. **96**, 157602 (2006).
[28] D. Fuchs, M. Adam, P. Schweiss, S. Gerhold, S. Schuppler, R. Schneider, and B. Obst, J. Appl. Phys. **88**, 1844 (2000).
[29] D. A. Tenne, A. Bruchhausen, N. D. Lanzillotti-Kimura, A. Fainstein, R. S. Katiyar, A. Cantarero, A. Soukiassian, V. Vaithyanathan, J. H. Haeni, W. Tian, D. G. Schlom, K. J. Choi, D. M. Kim, C. B. Eom, H. P. Sun, X. Q. Pan, Y. L. Li, L. Q. Chen, Q. X. Jia, S. M. Nakhmanson, K. M. Rabe, and X. X. Xi, Science **313**, 1614 (2006).
[30] W. G. Nilsen and J. G. Skinner, J. Chem. Phys. **48**, 2240 (1968).
[31] T. Ostapchuk, J. Petzelt, V. Železný, A. Pashkin, J. Pokorný, I. Drbohlav, R. Kužel, D. Rafaja, B. P. Gorshunov, M. Dressel, C. Ohly, S. Hoffmann-Eifert, and R. Waser, Phys. Rev. B **66**, 235406 (2002).
[32] J. Petzelt, I. Gregora, I. Rychetský, T. Ostapchuk, S. Kamba, P. Vaněk, Y. Yuzyuk, A. Almeida, M. R. Chavez, B. Gorshunov, M. Dressel, S. Hoffmann-Eifert, and R. Waser, J. Eur. Ceram. Soc. **21**, 2681 (2001).
[33] T. Suzuki, Y. Nishi, and M. Fujimoto, Philos. Mag. A **79**, 2461 (1999).
[34] T. Yamada, K. F. Astafiev, V. O. Sherman, A. K. Tagantsev, P. Muralt, and N. Setter, Appl. Phys. Lett. **86**, 142904 (2005).
[35] T. Yamada, K. F. Astafiev, V. Sherman, A. K. Tagantsev, D. Su, P. Muralt, and N. Setter, J. Appl. Phys. **98**, 054105 (2005).
[36] L. Arzel, B. Hehlen, A. K. Tagantsev, F. Dénoyer, K. D. Liss, R. Currat, and E. Courtens, Ferroelectrics **267**, 317 (2002).
[37] J. C. Slonczewski and H. Thomas, Phys. Rev. B **1**, 3599 (1970).
[38] Precisely, LAO has a hexagonal unit cell with $a = b = 5.364$ Å, $c = 13.111$ Å, consisting of perovskite sublattices. In this paper, the Miller index is referenced to the cubic perovskite sublattice.
[39] T. Yamada, T. Kiguchi, A. K. Tagantsev, H. Morioka, T. Iijima, H. Ohsumi, S. Kimura, M. Osada, N. Setter, and H. Funakubo, Integr. Ferroelectrics **115**, 57 (2010).
[40] A. K. Tagantsev, E. Courtens, and L. Arzel, Phys. Rev. B **64**, 224107 (2001).